Eur. Phys. J. C 34, 127–144 (2004)
Digital Object Identifier (DOI) 10.1140/epjc/s2004-01709-5

THE EUROPEAN PHYSICAL JOURNAL C

Measurement of the W-pair production cross-section and W branching ratios in e^+e^- collisions at $\sqrt{s} = 161$–209 GeV

The DELPHI Collaboration

J. Abdallah[25], P. Abreu[22], W. Adam[51], P. Adzic[11], T. Albrecht[17], T. Alderweireld[2], R. Alemany-Fernandez[8], T. Allmendinger[17], P. Allport[23], U. Amaldi[29], N. Amapane[45], S. Amato[48], E. Anashkin[36], A. Andreazza[28], S. Andringa[22], N. Anjos[22], P. Antilogus[25], W-D. Apel[17], Y. Arnoud[14], S. Ask[26], B. Asman[44], E. Augustin[25], A. Augustinus[8], P. Baillon[8], A. Ballestrero[46], P. Bambade[20], R. Barbier[27], D. Bardin[16], G. Barker[17], A. Baroncelli[39], M. Battaglia[8], M. Baubillier[25], K.-H. Becks[53], M. Begalli[6], A. Behrmann[53], E. Ben-Haim[20], N. Benekos[32], A. Benvenuti[5], C. Berat[14], M. Berggren[25], L. Bernztson[44], D. Bertrand[2], M. Besancon[40], N. Besson[40], D. Bloch[9], M. Blom[31], M. Bluj[52], M. Bonesini[29], M. Boonekamp[40], L. Booth[23], G. Borisov[21], O. Botner[49], B. Bouquet[20], V. Bowcock[23], I. Boyko[16], M. Bracko[43], R. Brenner[49], E. Brodet[35], P. Bruckman[18], M. Brunet[7], L. Bugge[33], P. Buschmann[53], M. Calvi[29], T. Camporesi[8], V. Canale[38], F. Carena[8], N. Castro[22], F. Cavallo[5], M. Chapkin[42], Ph. Charpentier[8], P. Checchia[36], R. Chierici[8], P. Chliapnikov[42], J. Chudoba[8], U. Chung[8], K. Cieslik[18], P. Collins[8], R. Contri[13], G. Cosme[20], F. Cossutti[47], J. Costa[50], D. Crennell[37], J. Cuevas[34], J. D'Hondt[2], J. Dalmau[44], T. da Silva[48], W. Da Silva[25], G. Della Ricca[47], A. De Angelis[47], W. De Boer[17], C. De Clercq[2], B. De Lotto[47], N. De Maria[45], A. De Min[36], L. de Paula[48], L. Di Ciaccio[38], A. Di Simone[39], K. Doroba[52], J. Drees[53,8], M. Dris[32], G. Eigen[4], T. Ekelof[49], M. Ellert[49], M. Elsing[8], C. Espirito Santo[22], G. Fanourakis[11], D. Fassouliotis[11,3], M. Feindt[17], J. Fernandez[41], A. Ferrer[50], F. Ferro[13], U. Flagmeyer[53], H. Foeth[8], E. Fokitis[32], F. Fulda-Quenzer[20], J. Fuster[50], M. Gandelman[48], C. Garcia[50], Ph. Gavillet[8], E. Gazis[32], R. Gokieli[8,52], B. Golob[43], G. Gomez-Ceballos[41], P. Goncalves[22], E. Graziani[39], G. Grosdidier[20], K. Grzelak[52], J. Guy[37], C. Haag[17], A. Hallgren[49], K. Hamacher[53], K. Hamilton[35], S. Haug[33], F. Hauler[17], V. Hedberg[26], M. Hennecke[17], H. Herr[8], J. Hoffman[52], S-O. Holmgren[44], J. Holt[8], A. Houlden[23], K. Hultqvist[44], N. Jackson[23], G. Jarlskog[26], P. Jarry[40], D. Jeans[35], K. Johansson[44], D. Johansson[44], P. Jonsson[27], C. Joram[8], L. Jungermann[17], F. Kapusta[25], S. Katsanevas[27], E. Katsoufis[32], G. Kernel[43], P. Kersevan[8,43], U. Kerzel[17], A. Kiiskinen[15], T. King[23], J. Kjaer[8], P. Kluit[31], P. Kokkinias[11], C. Kourkoumelis[3], O. Kouznetsov[16], Z. Krumstein[16], M. Kucharczyk[18], J. Lamsa[1], G. Leder[51], F. Ledroit[14], L. Leinonen[44], R. Leitner[30], J. Lemonne[2], V. Lepeltier[20], T. Lesiak[18], W. Liebig[53], D. Liko[51], A. Lipniacka[44], H. Lopes[48], M. Lopez[34], D. Loukas[11], P. Lutz[40], L. Lyons[35], J. MacNaughton[51], A. Malek[53], S. Maltezos[32], F. Mandl[51], J. Marco[41], R. Marco[41], B. Marechal[48], M. Margoni[36], J-C. Marin[8], C. Mariotti[8], A. Markou[11], C. Martinez-Rivero[41], J. Masik[12], N. Mastroyiannopoulos[11], F. Matorras[41], C. Matteuzzi[29], F. Mazzucato[36], M. Mazzucato[36], R. Mc Nulty[23], C. Meroni[28], E. Migliore[45], W. Mitaroff[51], U. Mjoernmark[26], T. Moa[44], M. Moch[17], K. Moenig[8,10], R. Monge[13], J. Montenegro[31], D. Moraes[48], S. Moreno[22], P. Morettini[13], U. Mueller[53], K. Muenich[53], M. Mulders[31], L. Mundim[6], W. Murray[37], B. Muryn[19], G. Myatt[35], T. Myklebust[33], M. Nassiakou[11], F. Navarria[5], K. Nawrocki[52], R. Nicolaidou[40], M. Nikolenko[16,9], A. Oblakowska-Mucha[19], V. Obraztsov[42], A. Olshevski[16], A. Onofre[22], R. Orava[15], K. Osterberg[15], A. Ouraou[40], A. Oyanguren[50], M. Paganoni[29], S. Paiano[5], P. Palacios[23], H. Palka[18], D. Papadopoulou[32], L. Pape[8], C. Parkes[24], F. Parodi[13], U. Parzefall[8], A. Passeri[39], O. Passon[53], L. Peralta[22], V. Perepelitsa[50], A. Perrotta[5], A. Petrolini[13], J. Piedra[41], L. Pieri[39], F. Pierre[40], M. Pimenta[22], E. Piotto[8], T. Podobnik[43], V. Poireau[8], E. Pol[6], G. Polok[18], P. Poropat[47], V. Pozdniakov[16], N. Pukhaeva[2,16], A. Pullia[29], J. Rames[12], L. Ramler[17], A. Read[33], P. Rebecchi[8], J. Rehn[17], D. Reid[31], R. Reinhardt[53], P. Renton[35], F. Richard[20], J. Ridky[12], M. Rivero[41], D. Rodriguez[41], A. Romero[45], P. Ronchese[36], P. Roudeau[20], T. Rovelli[5], V. Ruhlmann-Kleider[40], D. Ryabtchikov[42], A. Sadovsky[16], L. Salmi[15], J. Salt[50], A. Savoy-Navarro[25], U. Schwickerath[8], A. Segar[35], R. Sekulin[37], M. Siebel[53], A. Sisakian[16], G. Smadja[27], O. Smirnova[26], A. Sokolov[42], A. Sopczak[21], R. Sosnowski[52], T. Spassov[8], M. Stanitzki[17], A. Stocchi[20], J. Strauss[51], B. Stugu[4], M. Szczekowski[52], M. Szeptycka[52], T. Szumlak[19], T. Tabarelli[29], C. Taffard[23], F. Tegenfeldt[49], J. Timmermans[31], L. Tkatchev[16], M. Tobin[23], S. Todorovova[12], B. Tome[22], A. Tonazzo[29], P. Tortosa[50], P. Travnicek[12], D. Treille[8], G. Tristram[7], M. Trochimczuk[52], C. Troncon[28], M-L. Turluer[40], A. Tyapkin[16], P. Tyapkin[16], S. Tzamarias[11], V. Uvarov[42], G. Valenti[5], P. Van Dam[31], J. Van Eldik[8], A. Van Lysebetten[2], N. van Remortel[2], I. Van Vulpen[8], G. Vegni[28], F. Veloso[22], W. Venus[37], P. Verdier[27], V. Verzi[38], D. Vilanova[40], L. Vitale[47], V. Vrba[12], H. Wahlen[53], J. Washbrook[23], C. Weiser[17], D. Wicke[8], J. Wickens[2], G. Wilkinson[35], M. Winter[9], M. Witek[18], O. Yushchenko[42], A. Zalewska[18], P. Zalewski[52], D. Zavrtanik[43], V. Zhuravlov[16], I. Zimin[16], A. Zintchenko[16], M. Zupan[11]

[1] Department of Physics and Astronomy, Iowa State University, Ames IA 50011-3160, USA
[2] Physics Department, Universiteit Antwerpen, Universiteitsplein 1, 2610 Antwerpen, Belgium
and IIHE, ULB-VUB, Pleinlaan 2, 1050 Brussels, Belgium
and Faculté des Sciences, Univ. de l'Etat Mons, Av. Maistriau 19, 7000 Mons, Belgium
[3] Physics Laboratory, University of Athens, Solonos Str. 104, 10680 Athens, Greece
[4] Department of Physics, University of Bergen, Allégaten 55, 5007 Bergen, Norway
[5] Dipartimento di Fisica, Università di Bologna and INFN, Via Irnerio 46, 40126 Bologna, Italy
[6] Centro Brasileiro de Pesquisas Físicas, rua Xavier Sigaud 150, 22290 Rio de Janeiro, Brazil
and Depto. de Física, Pont. Univ. Católica, C.P. 38071 22453 Rio de Janeiro, Brazil
and Inst. de Física, Univ. Estadual do Rio de Janeiro, rua São Francisco Xavier 524, Rio de Janeiro, Brazil
[7] Collège de France, Lab. de Physique Corpusculaire, IN2P3-CNRS, 75231 Paris Cedex 05, France
[8] CERN, 1211 Geneva 23, Switzerland
[9] Institut de Recherches Subatomiques, IN2P3 - CNRS/ULP - BP20, 67037 Strasbourg Cedex, France
[10] Now at DESY-Zeuthen, Platanenallee 6, 15735 Zeuthen, Germany
[11] Institute of Nuclear Physics, N.C.S.R. Demokritos, P.O. Box 60228, 15310 Athens, Greece
[12] FZU, Inst. of Phys. of the C.A.S. High Energy Physics Division, Na Slovance 2, 180 40, Praha 8, Czech Republic
[13] Dipartimento di Fisica, Università di Genova and INFN, Via Dodecaneso 33, 16146 Genova, Italy
[14] Institut des Sciences Nucléaires, IN2P3-CNRS, Université de Grenoble 1, 38026 Grenoble Cedex, France
[15] Helsinki Institute of Physics, P.O. Box 64, 00014 University of Helsinki, Finland
[16] Joint Institute for Nuclear Research, Dubna, Head Post Office, P.O. Box 79, 101 000 Moscow, Russian Federation
[17] Institut für Experimentelle Kernphysik, Universität Karlsruhe, Postfach 6980, 76128 Karlsruhe, Germany
[18] Institute of Nuclear Physics,Ul. Kawiory 26a, 30055 Krakow, Poland
[19] Faculty of Physics and Nuclear Techniques, University of Mining and Metallurgy, 30055 Krakow, Poland
[20] Université de Paris-Sud, Lab. de l'Accélérateur Linéaire, IN2P3-CNRS, Bât. 200, 91405 Orsay Cedex, France
[21] School of Physics and Chemistry, University of Lancaster, Lancaster LA1 4YB, UK
[22] LIP, IST, FCUL - Av. Elias Garcia, 14-1^{o}, 1000 Lisboa Codex, Portugal
[23] Department of Physics, University of Liverpool, P.O. Box 147, Liverpool L69 3BX, UK
[24] Dept. of Physics and Astronomy, Kelvin Building, University of Glasgow, Glasgow G12 8QQ
[25] LPNHE, IN2P3-CNRS, Univ. Paris VI et VII, Tour 33 (RdC), 4 place Jussieu, 75252 Paris Cedex 05, France
[26] Department of Physics, University of Lund, Sölvegatan 14, 223 63 Lund, Sweden
[27] Université Claude Bernard de Lyon, IPNL, IN2P3-CNRS, 69622 Villeurbanne Cedex, France
[28] Dipartimento di Fisica, Università di Milano and INFN-MILANO, Via Celoria 16, 20133 Milan, Italy
[29] Dipartimento di Fisica, Univ. di Milano-Bicocca and INFN-MILANO, Piazza della Scienza 2, 20126 Milan, Italy
[30] IPNP of MFF, Charles Univ., Areal MFF, V Holesovickach 2, 180 00, Praha 8, Czech Republic
[31] NIKHEF, Postbus 41882, 1009 DB Amsterdam, The Netherlands
[32] National Technical University, Physics Department, Zografou Campus, 15773 Athens, Greece
[33] Physics Department, University of Oslo, Blindern, 0316 Oslo, Norway
[34] Dpto. Fisica, Univ. Oviedo, Avda. Calvo Sotelo s/n, 33007 Oviedo, Spain
[35] Department of Physics, University of Oxford, Keble Road, Oxford OX1 3RH, UK
[36] Dipartimento di Fisica, Università di Padova and INFN, Via Marzolo 8, 35131 Padua, Italy
[37] Rutherford Appleton Laboratory, Chilton, Didcot OX11 OQX, UK
[38] Dipartimento di Fisica, Università di Roma II and INFN, Tor Vergata, 00173 Rome, Italy
[39] Dipartimento di Fisica, Università di Roma III and INFN, Via della Vasca Navale 84, 00146 Rome, Italy
[40] DAPNIA/Service de Physique des Particules, CEA-Saclay, 91191 Gif-sur-Yvette Cedex, France
[41] Instituto de Fisica de Cantabria (CSIC-UC), Avda. los Castros s/n, 39006 Santander, Spain
[42] Inst. for High Energy Physics, Serpukov P.O. Box 35, Protvino, (Moscow Region), Russian Federation
[43] J. Stefan Institute, Jamova 39, 1000 Ljubljana, Slovenia and Laboratory for Astroparticle Physics, Nova Gorica Polytechnic, Kostanjeviska 16a, 5000 Nova Gorica, Slovenia,
and Department of Physics, University of Ljubljana, 1000 Ljubljana, Slovenia
[44] Fysikum, Stockholm University, Box 6730, 113 85 Stockholm, Sweden
[45] Dipartimento di Fisica Sperimentale, Università di Torino and INFN, Via P. Giuria 1, 10125 Turin, Italy
[46] INFN,Sezione di Torino, and Dipartimento di Fisica Teorica, Università di Torino, Via P. Giuria 1, 10125 Turin, Italy
[47] Dipartimento di Fisica, Università di Trieste and INFN, Via A. Valerio 2, 34127 Trieste, Italy
and Istituto di Fisica, Università di Udine, 33100 Udine, Italy
[48] Univ. Federal do Rio de Janeiro, C.P. 68528 Cidade Univ., Ilha do Fundão 21945-970 Rio de Janeiro, Brazil
[49] Department of Radiation Sciences, University of Uppsala, P.O. Box 535, 751 21 Uppsala, Sweden
[50] IFIC, Valencia-CSIC, and D.F.A.M.N., U. de Valencia, Avda. Dr. Moliner 50, 46100 Burjassot (Valencia), Spain
[51] Institut für Hochenergiephysik, Österr. Akad. d. Wissensch., Nikolsdorfergasse 18, 1050 Vienna, Austria
[52] Inst. Nuclear Studies and University of Warsaw, Ul. Hoza 69, 00681 Warsaw, Poland
[53] Fachbereich Physik, University of Wuppertal, Postfach 100 127, 42097 Wuppertal, Germany

Received: 13 November 2003 / Revised version: 21 January 2004 /
Published online: 9 March 2004 –

Abstract. These final results on $e^+e^- \to W^+W^-$ production cross-section measurements at LEP2 use data collected by the DELPHI detector at centre-of-mass energies up to 209 GeV. Measurements of total cross-sections, W angular differential distributions and decay branching fractions, and the value of the CKM element $|V_{cs}|$ are compared to the expectations of the Standard Model. These results supersede all values previously published by DELPHI.

1 Introduction

The cross-section for the doubly resonant production of W bosons has been measured with the data sample collected with the DELPHI detector during the high-energy operation phase of the LEP e^+e^- collider (LEP2), at centre-of-mass energies from 161 GeV up to 209 GeV. Measurements of total cross-sections, W angular differential distributions and decay branching fractions, and the value of the CKM element $|V_{cs}|$ are presented. They are compared to the Standard Model including most recent theoretical predictions [1].

The cross-sections determined in these analyses correspond to W pair production, defined through the three doubly resonant tree-level diagrams ("CC03 diagrams" [2] in the following) involving s-channel γ and Z exchange and t-channel ν exchange, as shown in Fig. 1. Depending on the decay mode of each W, fully hadronic, mixed hadronic-leptonic ("semi-leptonic") or fully leptonic final states are obtained.

This paper is organised as follows: after a brief description of the DELPHI detector in Sect. 2, a summary of the analysed data and simulation samples is provided in Sect. 3. Track selection and particle identification are briefly illustrated in Sect. 4 and in Sect. 5 the selection of WW events is described and the performance of the analysis reported; Sect. 6 is devoted to the discussion of the systematic error assessment. In Sects. 7 and 8, results in terms of differential cross-sections, total cross-section and W branching ratios are presented. In Sect. 9 the results are compared to the theoretical predictions and conclusions follow in Sect. 10.

2 The DELPHI detector in the LEP2 phase

The DELPHI detector configuration for LEP1 running was described elsewhere [3]. For operation at LEP2, changes were made to the subdetectors, the trigger system [4], the run control and the algorithms used in the offline reconstruction of charged particles, which improved the performance compared to LEP1.

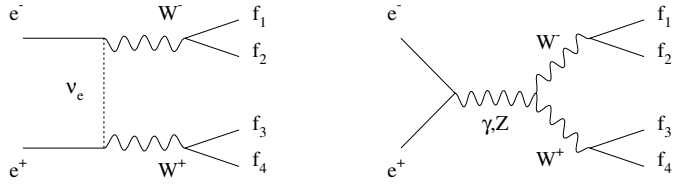

Fig. 1. CC03 diagrams

The major changes were the extension of the Vertex Detector (VD) and the inclusion of the Very Forward Tracker (VFT) [5], which enlarged the coverage of the silicon tracker out to $11^\circ < \theta < 169^\circ$[1]. Also the Inner Detector, both the Jet Chamber and Trigger Layers, were extended to cover the polar angle region $15^\circ < \theta < 165^\circ$. Together with improved tracking algorithms, alignment and calibration procedures optimised for LEP2, these changes led to an improved track reconstruction efficiency in the forward regions.

Changes were made to the electronics of the trigger and timing system which improved the stability of the running during data taking. The trigger conditions were optimised for LEP2 running, to give high efficiency for Standard Model two-fermion and four-fermion processes and also give sensitivity to events which may be signatures of new physics. In addition, improvements were made to the operation of the detector during the LEP cycle, to prepare the detector for data taking at the very start of stable collisions of the beams, and to respond to adverse background conditions from LEP were they to arise. These changes led to an overall improvement of $\sim 10\%$ in the efficiency for collecting the delivered luminosity, from $\sim 85\%$ at the start of LEP2 in 1995 to $\sim 95\%$ at the end in year 2000.

During the operation of the detector in year 2000 one of the sectors representing 1/12 of the acceptance of the central tracking device, the Time Projection Chamber (TPC), failed. This problem affects about a quarter of the data collected in that year. Nevertheless, the redundancy of the tracking system meant that charged particles passing through the sector could still be reconstructed from signals in other tracking detectors. A modified track reconstruction algorithm was used in this sector, which included space points reconstructed in the Barrel RICH detector, helpful in the determination of the polar angle of charged particles. As a result, the track reconstruction efficiency was only slightly reduced in the region covered by the broken sector. The impact of the failure of this part of the detector on the analyses is discussed further in Sect. 6.1.

3 Data and simulation samples

A summary of the data samples used for the WW cross-section measurement is reported in Table 1, where the lu-

[1] The DELPHI coordinate system has the z-axis collinear with the incoming electron beam. θ indicates the polar angle with respect to the z-axis, $R\phi$ indicates the plane perpendicular to the z axis.

Table 1. Integrated luminosity-weighted centre-of-mass energies and luminosities in the LEP2 data taking period. The hadronic luminosity is used for the four-quark channel, the leptonic one for the semi-leptonic and fully leptonic channels

Year	$\mathcal{L}$-weighted $\sqrt{s}$ (GeV)	Hadronic $\mathcal{L}$ (pb^{-1})	Leptonic $\mathcal{L}$ (pb^{-1})
1996	161.31	10.07	10.07
	172.14	10.12	10.12
1997	182.65	52.51	51.63
1998	188.63	154.35	153.81
1999	191.58	25.16	24.51
	195.51	76.08	71.99
	199.51	82.79	81.82
	201.64	40.31	39.70
2000	204.81	82.63	74.93
	206.55	135.82	123.66

minosity-weighted centre-of-mass energies and the amount of data analysed at each energy are shown. The luminosity is determined from Bhabha scattering measurements making use of the very forward electromagnetic calorimetry [6]. The total integrated luminosity for the LEP2 period corresponds approximately to 670 pb^{-1}. The luminosities used for the different selections correspond to those data for which all elements of the detector essential to each specific analysis were fully functional; tighter requirements on the detectors used for lepton identification were applied for the data samples used in the semi-leptonic and fully leptonic channel analyses. The luminosity in year 2000 was delivered in a continuum of energies, thus data taken during this period are divided into two centre-of-mass energy ranges, above and below 205.5 GeV, referred to as 205 GeV and 207 GeV in the following.

All the data taken from the year 1997 onwards have been reprocessed with an updated version of the DELPHI reconstruction software, using a consistent treatment for all the samples. Larger simulation samples were realised with more up-to-date Monte Carlo programs, interfaced to the full DELPHI simulation program DELSIM [3] and reconstructed with the same reconstruction program as the real data.

The cross-section analyses on these data are updated with respect to the previously published ones [7] and supersede them. The data taken in year 1996 have not been reanalysed, because possible improvements were negligible compared to the large statistical errors of those measurements; these results correspond to the publications in [9], with a revised determination of the luminosity [8].

Four-fermion simulation samples were produced with the WPHACT [10] generator, interfaced with the PYTHIA 6.156 [11] hadronisation model. In order to perform checks on hadronisation effects, the same generator was also interfaced to the ARIADNE [12] and HERWIG [13] hadronisation models.

The generation was complemented with two-photon collision generators BDK [14], BDKRC [15] and PYTHIA. The most recent $\mathcal{O}(\alpha)$ electroweak corrections, via the so-called Leading Pole Approximation (LPA), were included in our generation of the signal via weights given by the YFSWW program [16], according to the scheme described in [17].

The selection efficiencies were defined with respect to the CC03 diagrams only, by reweighting each event to the CC03 contribution according to the ratio of the squared matrix elements computed with these diagrams only and with the full set of diagrams.

The simulation of two-fermion background processes was realised with the KK2f [18] and KoralZ [19] generators interfaced to PYTHIA, ARIADNE and HERWIG, for which the fragmentation parameters have been tuned at the Z-resonance [20], and the BHWIDE [21] generator for Bhabha events.

4 Charged particle selection and lepton identification

To improve the event reconstruction and reject contributions from either cosmic ray events, beam-gas interactions or noise from electronics, the reconstructed charged particles were required to fulfil the following criteria:

- momentum 0.1 GeV/c $<$p$<$ 1.5 $\cdot$ $\mathrm{P_{beam}}$;
- momentum error Δp/p$<$ 1;
- $R\phi$ impact parameter < 4 cm;
- z impact parameter $< 4\,\mathrm{cm}/\sin\theta$.

Tracks seen by only the central tracking devices (Vertex Detector (VD) and Inner Detector (ID)) were rejected if no z coordinate measurement was available.

Neutral clusters of energy in the barrel (HPC), forward (FEMC) and very forward (STIC) electromagnetic calorimeters were required to have an energy of at least 300, 400 and 300 MeV respectively. In addition, off–momentum electrons in the STIC were rejected by a cut on the polar angle of a shower at 3°. Noise from the hadron calorimeter (HCAL) was reduced by rejecting showers which had activity in only one layer and failed a selection based on energy, number of hits and longitudinal position.

Muon identification was performed by extrapolating tracks through the entire detector, and associating nearby HCAL energy deposits and muon chamber hits to the tracks. The errors on track parameters, on the energy deposits and on the position of chamber hits were taken into account when making this association. Particles were identified as muons if there was at least one muon chamber hit associated to a track or if the size and longitudinal profile of the HCAL energy deposits associated to a track were consistent with a minimum ionizing particle.

Electron identification was based on the reconstructed showers in the electromagnetic calorimeters associated to charged particle tracks. The barrel photons in a conic region close to the direction of the track were reassociated to the candidate electron, also accounting for the bending caused by the magnetic field. A particle was identified as an electron if the associated calorimetric energy was larger than 50% of the momentum reconstructed in magnetic field. For tracks below 30 GeV/c, the identification algorithm was based on a combination of the energy-momentum ratio, the measurement of the energy loss in the TPC, the matching of the track to the shower in the z and ϕ directions and on the shower profile. FEMC electromagnetic deposits close in space were clustered together and the association with reconstructed tracks was used for electron/photon discrimination. Care was taken in excluding those tracks which were likely to come from the development of a shower outside the calorimeter. In addition, the ratio between the electromagnetic energy and the total energy (electromagnetic and hadronic) was required to be above 90%. For energetic and isolated tracks in the regions not covered by electromagnetic calorimetry, the measurement of the energy loss in the TPC was used. The estimate of electron energy was obtained from a combination of the track momentum and the calorimetric deposition.

5 Event selection and partial cross-sections

5.1 Fully hadronic final state

5.1.1 Selection of fully hadronic final state events

For the selection of $\mathrm{W^+W^-} \to q\bar{q}q\bar{q}$, the charged and neutral particles in each event were forced into a four-jet configuration with the DURHAM algorithm [22]. A preselection of events was performed to select well reconstructed hadronic events without missing energy and momentum. The following conditions were imposed:

- reconstructed effective centre-of-mass energy [23] $\sqrt{s'} > 65\%$ of the nominal centre-of-mass energy;
- total and transverse energy for charged particles, $E_{ch} = \sum_{i=1}^{N} E_i^{ch}$ and $E_t = \sum_i \mid p_t^i \mid$, where p_t^i is the momentum component of the particle i perpendicular to the beam axis, each $> 20\%$ of nominal centre-of-mass energy;
- total particle multiplicity ≥ 3 for each jet;
- $y_{\mathrm{cut}} > 0.0006$ for the migration from 4 to 3 jets when clustering with the DURHAM algorithm;
- convergence of a four-constraint (4C) fit of the measured jet energies and directions imposing four-momentum conservation.

A feed-forward neural network was then used to improve the rejection of two-fermion (mainly $\mathrm{Z}/\gamma \to q\bar{q}(g)$) and four-fermion background (mainly $\mathrm{ZZ} \to q\bar{q}q\bar{q}, q\bar{q}\tau^+\tau^-$). The network, based on the JETNET package [24], uses the standard back-propagation algorithm and consists of three layers with 13 input nodes, 7 hidden nodes and one output node.

The following jet and event observables were chosen as input variables, taking into account previous neural network studies [25] to optimise input variables for the WW and two-fermion separation:

- the difference between the maximum and minimum jet energies after the 4C fit;
- the minimum angle between two jets after the 4C fit;
- the value of y_{cut} from the DURHAM algorithm for the migration of 4 jets into 3 jets;
- the minimum particle multiplicity of any jet;
- the reconstructed effective centre-of-mass energy $\sqrt{s'}$;
- the maximum probability, amongst the three possible jet pairings, for a 6C fit (imposing 4-momentum conservation and the invariant mass of each jet pair equal to the W-mass);
- the thrust;
- the sphericity;
- the transverse energy;
- the sum of the cubes of the magnitudes of the momenta of the 7 highest momentum particles $\sum_{i=1}^{7} |\mathbf{p}_i|^3$;
- the minimum jet broadening B_{min} [22];
- the Fox-Wolfram-moment H3 [26];
- the Fox-Wolfram-moment H4.

The neural network was trained separately at each energy. Each training was performed with 2500 signal events and 2500 $\mathrm{Z}/\gamma \to q\bar{q}$ background events. Afterwards the network output was calculated for other independent samples of simulated four-fermion, Z/γ and $\gamma\gamma$ events, and for the data. Figure 2 shows distributions of the neural network output for data and simulated events at 189 and 207 GeV.

Events were selected by applying a cut on the NN output variable, chosen to minimise the total error on the measured cross-section including the systematic uncertainty on the two-fermion background with its correlation at all centre-of-mass energies (see Sect. 6).

5.1.2 Results for fully hadronic final state

The efficiency and background contamination for the hadronic event selections were evaluated independently at the different centre-of-mass energies. The selection performance at $\sqrt{s} = 200$ GeV and the total number of events selected in each data sample are reported in Table 2. The efficiencies varied by no more than 4% over the different energy points above 172 GeV. The background is dominated by $\mathrm{qq}(\gamma)$, representing 70–75% of the contamination, decreasing with energy.

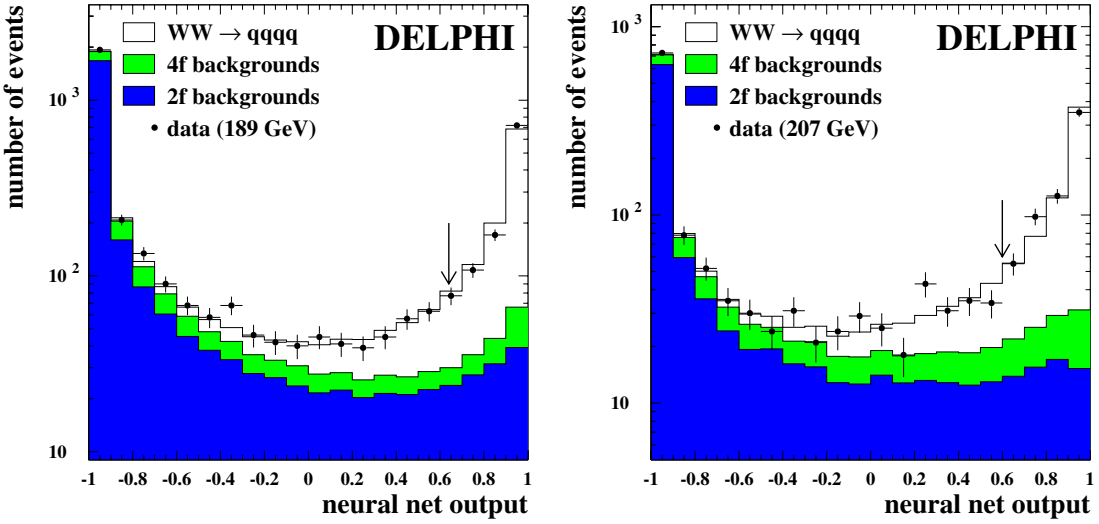

Fig. 2. Distribution of the Neural Network output variable for four-jet events at the centre-of-mass energies of 189 GeV and 207 GeV. The period of bad TPC operating conditions is excluded from the plot. The points show the data and the histograms are the predicted distributions for signal and background. The arrows indicate the cut value applied for the selection of events

Table 2. Data for the cross-section measurement of hadronic and semi-leptonic final states. The efficiency matrix and the backgrounds are the ones at 200 GeV. The backgrounds include two-fermion and non-CC03 four-fermion contributions. The upper limits on the efficiencies are at the 95% C.L.

	efficiencies for selected channels			
channel	$jjjj$	$jje\nu$	$jj\mu\nu$	$jj\tau\nu$
$q\bar{q}q\bar{q}$	**0.797**	$< 10^{-4}$	$< 10^{-4}$	0.012
$q\bar{q}e\nu$	0.004	**0.677**	0.004	0.114
$q\bar{q}\mu\nu$	0.002	0.001	**0.852**	0.043
$q\bar{q}\tau\nu$	0.016	0.032	0.026	**0.581**
background (pb)	1.21	0.232	0.075	0.371
$\sqrt{s}$ (GeV)	Selected events			
161	15		12	
172	65	14	17	14
183	345	94	118	123
189	1042	269	336	339
192	187	42	53	58
196	532	151	166	164
200	614	162	190	208
202	317	94	89	83
205	657	169	153	174
207	999	214	259	289
All	4773		4054	

At each energy point the cross-section for fully hadronic events was obtained from a binned maximum likelihood fit to the distribution of the NN output variable above the cut value, assuming Poissonian probability density functions for the number of events. The probability is calculated on the basis of the efficiency for being reconstructed in a given bin of the NN output and the expected background in each bin and is a function of the partial cross-section to be measured. For this fit the contamination from other WW channels, with its value fixed to the SM prediction, was considered as a background.

Table 3. Measured hadronic cross-sections

$\sqrt{s}$ (GeV)	$\sigma_{\mathrm{WW}}^{qqqq} = \sigma_{\mathrm{WW}} \times \mathrm{BR}(\mathrm{WW} \to q\bar{q}q\bar{q})$ (pb)
161	$1.53^{+0.67}_{-0.55}$ (stat) $\pm$ 0.13 (syst)
172	$4.65^{+0.95}_{-0.86}$ (stat) $\pm$ 0.18 (syst)
183	7.23 ± 0.45 (stat) ± 0.09 (syst)
189	7.38 ± 0.27 (stat) ± 0.09 (syst)
192	7.78 ± 0.68 (stat) ± 0.10 (syst)
196	7.69 ± 0.39 (stat) ± 0.10 (syst)
200	7.73 ± 0.37 (stat) ± 0.10 (syst)
202	7.83 ± 0.54 (stat) ± 0.10 (syst)
205	8.26 ± 0.38 (stat) ± 0.10 (syst)
207	7.59 ± 0.29 (stat) ± 0.10 (syst)

The results for $\sigma_{\mathrm{WW}}^{q\bar{q}q\bar{q}} = \sigma_{\mathrm{WW}} \times \mathrm{BR}(\mathrm{WW} \to q\bar{q}q\bar{q})$, where $\mathrm{BR}(\mathrm{WW} \to q\bar{q}q\bar{q})$ is the probability for the W-pair to give a purely hadronic final state, are reported in Table 3. Systematic uncertainties were determined as detailed in Sect. 6.

5.2 Semi-leptonic final state

5.2.1 Selection of semi-leptonic final state events

Events in which one of the W bosons decays into a lepton and a neutrino and the other one into quarks are characterised by two or more hadronic jets, one isolated lepton (coming either directly from the W decay or from the cascade decay $\mathrm{W} \to \tau\nu_\tau \to e\nu_e\nu_\tau\nu_\tau$ *or* $\mu\nu_\mu\nu_\tau\nu_\tau$) or a low multiplicity jet due to a hadronic τ decay, and missing momentum resulting from the neutrino(s). The major

Table 4. Semi-leptonic preselection cuts. E_{train} indicates the centre-of-mass energy chosen for the training of the IDA (see text). The W mass is fitted through a constrained fit of the measured jets, lepton and unobserved neutrino imposing four-momentum conservation and the equality of the two W masses in the event

	$q\bar{q}e\nu/q\bar{q}\mu\nu$	$q\bar{q}\tau\nu$
Transverse energy (GeV)	> 45	> 40
Missing momentum (GeV/c)	> 10	$10<p_{mis}<80$
Visible energy/E_{train} (%)	$40<E/E_{train}<110$	$35<E/E_{train}<100$
Fitted W mass (GeV/c^2)	> 50	> 50

background comes from $q\bar{q}(\gamma)$ production and from four-fermion final states containing two quarks and two leptons of the same flavour.

Events were first required to pass a general hadronic preselection:

- at least 5 charged particles;
- energy of charged particles at least 10% of total centre-of-mass energy;
- $\sqrt{EMF_f^2 + EMF_b^2} < 0.9\times E_{\rm beam}$, where $EMF_{f,b}$ identify the total energy deposited in electromagnetic calorimeters in the forward and backward directions, defined as two 20° cones around the beam axes.

A search for leptons was then made. Of the identified electrons with an energy greater than 5 GeV, the one with the highest value of (energy $\times$ $\theta_{\rm iso}$) [2] was considered to be the electron candidate. This candidate was required to have an energy of at least 15 GeV. Of the identified muons with a momentum greater than 5 GeV/c, the one with the highest value of (momentum $\times$ $\theta_{\rm iso}$) was considered to be the muon candidate. This candidate was required to have a momentum of at least 15 GeV/c. The event was then clustered into jets using the LUCLUS [11] algorithm with a $d_{\rm join}$ value of 6.5 GeV/c. The resulting jets were trimmed by removing particles at an angle greater than 20° to the highest energy particle in the jet. Of these trimmed jets, the one with the smallest momentum–weighted spread [3] was taken to be the tau candidate. Particles with momenta smaller than 1 GeV/c were removed from the candidate jet if they were at an angle greater than 8° to the jet axis. At the end of the procedure, this jet was required to still contain at least one charged particle.

An event could have up to three lepton candidates, one of each flavour.

For each lepton candidate, all particles other than the lepton were clustered into two jets using the DURHAM algorithm. These two jets were required to contain at least three particles, at least one of which had to be charged. Additional preselection cuts are listed in Table 4: these reject most events due to photon–photon collisions, some events for which there is no missing energy, and events whose topologies are far from those of WW events.

After these preselection cuts, the final selection was made with an Iterative Discriminant Analysis (IDA) [27]. The standard IDA technique assumes that the signal and background distributions in the multi-observable space have different means but identical shapes. IDA was extended to treat correctly cases when the distributions have different shapes. The input observables were transformed to make their distributions Gaussian. The IDA selection was made in three channels ($q\bar{q}\mu\nu$, $q\bar{q}e\nu$ and $q\bar{q}\tau\nu$). The training was performed on Monte Carlo samples: around 50k events each of four-fermion charged and neutral current processes, and 100k $q\bar{q}(\gamma)$ events. The IDA was trained at three centre-of-mass energies: 189, 200 and 206 GeV.

The observables used in the discriminants are summarised in Table 5, and can be grouped into four categories:

- event observables such as the multiplicity, visible and transverse energies, aplanarity[4] and the reconstructed effective centre-of-mass energy ($\sqrt{s'}$) are useful to dis-

Table 5. Observables in semi-leptonic channels used in IDA analysis

	$q\bar{q}e\nu$	$q\bar{q}\mu\nu$	$q\bar{q}\tau\nu$
total multiplicity	X	X	X
visible energy	X	X	X
transverse energy	X		
aplanarity			X
$\sqrt{s'}/\sqrt{s}$	X	X	X
lepton energy	X	X	
lepton isolation angle	X	X	X
tau jet charged multiplicity			X
tau jet momentum–weighted spread			X
magnitude of missing momentum	X	X	X
polar angle of missing momentum	X	X	X
lepton–missing momentum angle		X	X
Fitted W mass	X	X	X

[2] The isolation angle $\theta_{\rm iso}$ is defined as the angle made to the closest charged particle with a momentum greater than 1 GeV/c.

[3] Defined as $\sum_i(\theta_i\cdot|p_i|)/\sum_i|p_i|$, where θ_i is the angle made by the momentum p_i of the i^{th} particle in the jet with the total jet momentum

[4] The aplanarity is defined as $\frac{3}{2}\lambda_3$, where λ_3 is the smallest eigenvalue of the sphericity tensor $S^{\alpha\beta} = \frac{\sum_i p_i^\alpha p_i^\beta}{\sum_i |\mathbf{p}_i|^2}$. The p_i are the 3-momenta of particles in the event, and $\alpha, \beta = 1, 2, 3$ correspond to the x, y, z momentum components.

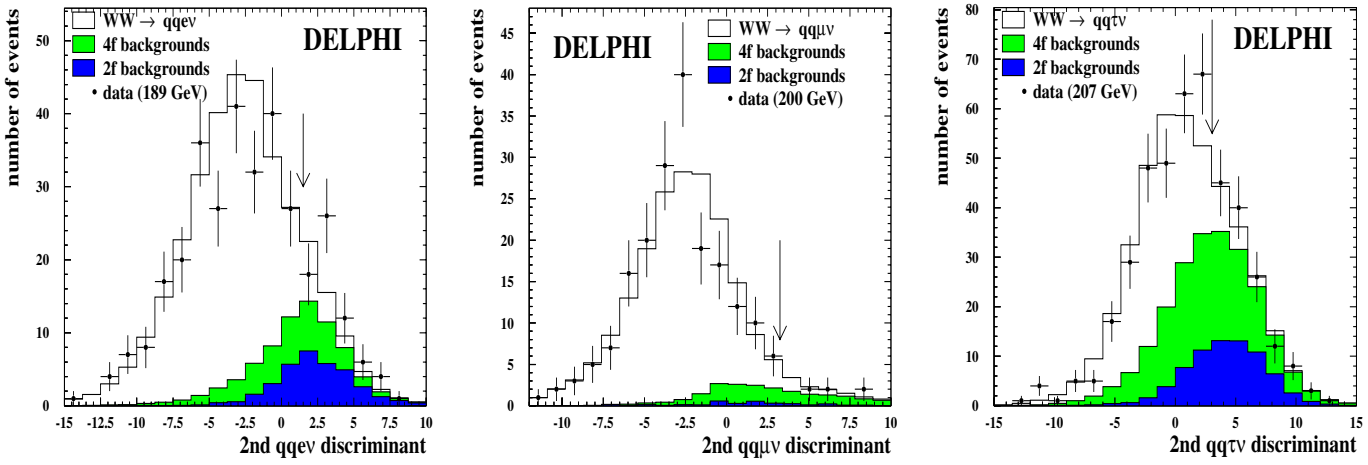

Fig. 3. Distribution of discriminants for the semi-leptonic selection. The plots refer to the $q\bar{q}e\nu$ selection at 189 GeV, the $q\bar{q}\mu\nu$ selection at 200 GeV and the $q\bar{q}\tau\nu$ selection at 207 GeV. The arrows indicate the cut value applied for the selection of events. The points show the data and the histograms are the predicted distributions for signal and background

tinguish between semi-leptonic and other four-fermion events, and to remove $q\bar{q}(\gamma)$ events, particularly those in the radiative return peak;
- observables concerned with the charged lepton (energy, isolation angle, tau jet multiplicity) are useful in discriminating between events with primary leptons and those with leptons originating in quark decays or in other processes, such as photon conversion;
- properties of the missing momentum (magnitude and polar angle) make use of the fact that the missing momentum from unseen initial state radiation (ISR in what follows) photons is directed along the beampipe;
- the angles between the lepton and missing momentum, and the fitted W mass from a constrained kinematic fit (imposing four-momentum conservation and the equality of the two W masses in the event) are sensitive to the event topologies expected from semi-leptonic WW decays.

The performance of the selection was measured using samples independent from those on which the training was performed. Events were selected with a cut on the output of the IDA, chosen to optimise the product of efficiency and purity for each channel. Events were first passed to the $q\bar{q}\mu\nu$ selection; if they were not selected, they were passed to the $q\bar{q}e\nu$; if they were still not selected, they were then finally passed to the $q\bar{q}\tau\nu$ selection.

Distributions of discriminants for the semi-leptonic event selection are shown in Fig. 3.

5.2.2 Results for semi-leptonic final state

The efficiency matrices and background contaminations for the semi-leptonic event selections were evaluated independently at the different centre-of-mass energies. The efficiencies differed by no more than 2% over the different energy points. The values at 200 GeV, with the number of events observed at each energy point are reported in Table 2. The final efficiencies for identifying $q\bar{q}e\nu$, $q\bar{q}\mu\nu$ and $q\bar{q}\tau\nu$ events with any of the three semi-leptonic selections at 200 GeV were 79.6%, 89.6% and 63.9% respectively. The background in all the channels was composed of two- and four-fermion events in similar proportions.

Table 6. Measured semi-leptonic cross-sections

$\sqrt{s}$ (GeV)	$\sigma_{\mathrm{WW}}^{qql\nu} = \sigma_{\mathrm{WW}} \times \mathrm{BR}(\mathrm{WW} \to q\bar{q}l\nu)$ (pb)
161	$1.74^{+0.67}_{-0.55}$ (stat) $\pm$ 0.10 (syst)
172	$5.68^{+1.02}_{-0.93}$ (stat) $\pm$ 0.17 (syst)
183	7.25 $\pm$ 0.46 (stat) $\pm$ 0.08 (syst)
189	6.89 $\pm$ 0.26 (stat) $\pm$ 0.08 (syst)
192	6.88 $\pm$ 0.64 (stat) $\pm$ 0.08 (syst)
196	7.50 $\pm$ 0.39 (stat) $\pm$ 0.08 (syst)
200	7.82 $\pm$ 0.37 (stat) $\pm$ 0.08 (syst)
202	7.71 $\pm$ 0.53 (stat) $\pm$ 0.08 (syst)
205	7.45 $\pm$ 0.38 (stat) $\pm$ 0.08 (syst)
207	6.95 $\pm$ 0.29 (stat) $\pm$ 0.08 (syst)

The number of events observed in the different lepton channels was found to be consistent with lepton universality. With this assumption, likelihood fits to the Poisson probability of the expected number of events, where the contamination of the fully hadronic channel is considered as background, yield the cross-sections $\sigma_{\mathrm{WW}}^{qql\nu} = \sigma_{\mathrm{WW}} \times \mathrm{BR}(\mathrm{WW} \to q\bar{q}l\nu)$ reported in Table 6. Systematic uncertainties were determined as detailed in Sect. 6.

5.3 Fully leptonic final state

5.3.1 Selection of fully leptonic final state event

Events in which both W bosons decay into $l\nu$ are characterised by low multiplicity, a clean two-particle (or jet from τ decay) topology with two energetic, acollinear leptons of opposite charge, acoplanar with the beam and with large missing momentum and energy. The relevant backgrounds

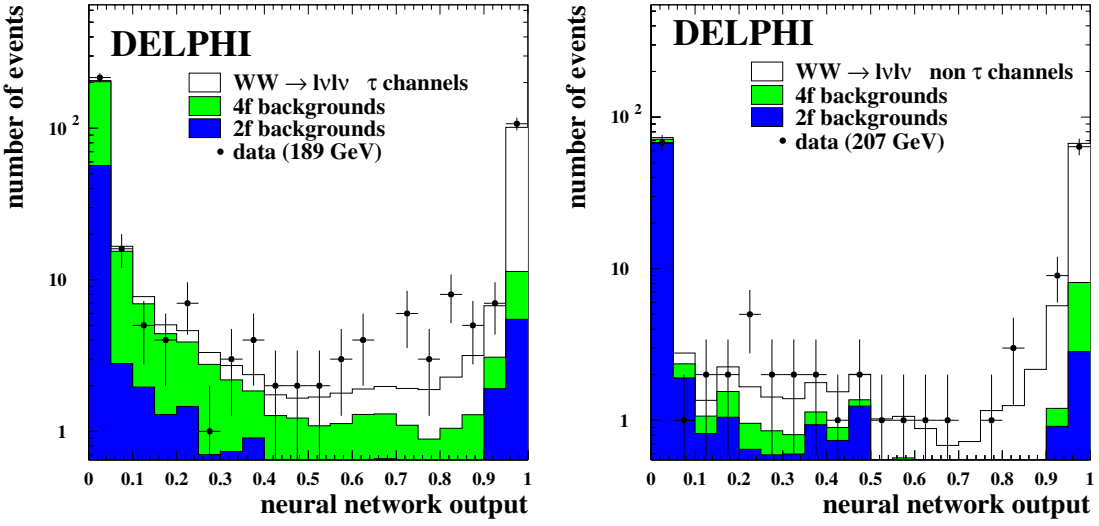

Fig. 4. Distribution of the output variable of the two types of Neural Network used for the selection of fully-leptonic events. The points show the data and the histograms are the predicted distributions for signal and background

are di-leptons from $e^+e^- \to \mathrm{Z}(\gamma)$, Bhabha scattering, two-photon collisions and leptonic final states from Z-pair and single boson production.

The selection was performed in three steps. First a leptonic preselection was made, followed by particle identification. Finally two Neural Networks were used to reject the remaining background.

An initial set of cuts was applied to select a sample enriched in leptonic events. All particles in the event were clustered into "jets" using the LUCLUS algorithm ($d_{\mathrm{join}} = 6.5\,\mathrm{GeV}/c$) and only events with two reconstructed jets, containing at least one charged particle each, were retained. A total charged particle multiplicity between 2 and 6 was required and at least one jet had to have only one charged particle. In order to reduce the background from two-photon collisions and radiative di-lepton events, the event acoplanarity, θ_{acop}, defined as the acollinearity of the two jet directions projected onto the plane perpendicular to the beam axis, had to be above 3°. In addition, the total momentum transverse to the beam direction, P_t, had to exceed 2% of the centre-of-mass energy $\sqrt{s}$. The associated energy deposited in the electromagnetic calorimeters for both leading particles (the ones with the largest momenta) was required to be less than $0.44 \cdot \sqrt{s}$ to reject Bhabha scattering. To reject radiative events further, the energy of the most energetic photon had to be less than $0.25 \cdot \sqrt{s}$ and the angle in the plane perpendicular to the beam axis between the charged particles system and the most energetic photon was required to be less than 170°. Finally, the energy of the charged particles in each jet had to be greater than $0.04 \cdot \sqrt{s}$ and the visible energy of the particles with $|\cos\theta| < 0.9$ had to exceed $0.06 \cdot \sqrt{s}$.

In events passing this selection each particle was classed as μ, e or hadron. A lepton was identified as a cascade decay from $\mathrm{W} \to \tau\nu_\tau$ if the momentum was lower than $0.13 \cdot \sqrt{s}$.

After the preselection and the channel identification, two Neural Networks based on the Multi Layer Perceptron (MLP) [28] package were built to reject the remaining background. They consisted of one output layer from 13 input variables, normalised to lie in the region between zero and one.

One of the two Neural Networks was tuned for the $\tau\nu_\tau X\nu_X$ channels ($X = e, \mu, \tau$) and the other for the remaining channels, given the different characteristics of the two samples. This was found to optimise the performance of the selection.

The following variables were used in both Neural Networks:

- the event acoplanarity;
- the event acollinearity;
- the larger of the associated energy from electromagnetic calorimetry of the two leptons;
- the transverse momentum, p_t;
- the transverse energy;
- the angle in the plane perpendicular to the beam axis between the vector sum of the charged particle momenta and the most energetic photon;
- the absolute value of the cosine of the polar angle of the missing momentum;
- the energy in the calorimeters not associated to charged particles outside two cones of 20° around both leading charged particles;
- the larger of the energies of the two jets coming from charged particles;
- the total energy of neutral particles;
- the larger of the invariant masses of the two jets;
- the total visible energy;
- the total energy of charged particles.

Distributions of the Neural Network output variable for the fully leptonic event selection are shown in Fig. 4. The cut applied on the Neural Network output was tuned in order to optimise the product of efficiency and purity. The cut was channel dependent, but did not depend on the centre-of-mass energy.

Table 7. Data for the cross-section measurement of the fully leptonic final state. The efficiency matrix and the background are the ones at 200 GeV. The upper limits on the efficiencies are at 95% C.L.

	efficiencies for selected channels					
channel	$\tau\nu\tau\nu$	$e\nu\tau\nu$	$\mu\nu\tau\nu$	$e\nu e\nu$	$e\nu\mu\nu$	$\mu\nu\mu\nu$
$\tau\nu\tau\nu$	**0.272**	0.087	0.077	0.004	0.008	0.006
$e\nu\tau\nu$	0.068	**0.462**	0.005	0.044	0.049	$< 2 \cdot 10^{-3}$
$\mu\nu\tau\nu$	0.042	0.004	**0.536**	$< 2 \cdot 10^{-3}$	0.061	0.053
$e\nu e\nu$	0.017	0.151	$< 10^{-3}$	**0.471**	$< 10^{-3}$	$< 2 \cdot 10^{-3}$
$e\nu\mu\nu$	0.012	0.041	0.094	$< 2 \cdot 10^{-3}$	**0.621**	$< 10^{-3}$
$\mu\nu\mu\nu$	0.008	$< 10^{-3}$	0.109	$< 2 \cdot 10^{-3}$	0.003	**0.677**
background (pb)	0.030	0.046	0.023	0.042	0.019	0.027
$\sqrt{s}$ (GeV)	Selected events					
161				2		
172				8		
183	4	13	10	9	9	14
189	22	56	43	25	45	38
192	4	2	14	4	8	7
196	16	29	19	12	24	7
200	12	26	28	11	27	13
202	4	20	13	4	6	9
205	14	26	22	7	24	10
207	14	40	41	16	44	16
All				891		

5.3.2 Results for fully leptonic final state

The efficiencies and backgrounds for $\sqrt{s} = 200\,\text{GeV}$ together with the numbers of selected events at each of the centre-of-mass energies are shown in Table 7. The overall $l\nu l\nu$ efficiency was 67.3% and the residual background from non-W and single-W events was 0.187 pb. The efficiencies were checked to be constant within 1–2% at the different energy points above 172 GeV. The number of observed events in each subchannel is consistent with the hypothesis of lepton universality. Table 8 presents the values, at each energy, of $\sigma_{\text{WW}}^{l\nu l\nu} = \sigma_{\text{WW}} \times \text{BR}(\text{WW} \to l\nu l\nu)$ from maximum likelihood fits to the Poisson probability of the expected number of events. Systematic uncertainties were determined as detailed in Sect. 6.

Table 8. Measured fully leptonic cross-sections

$\sqrt{s}$ (GeV)	$\sigma_{\text{WW}}^{l\nu l\nu} = \sigma_{\text{WW}} \times \text{BR}(\text{WW} \to l\nu l\nu)$ (pb)
161	$0.30^{+0.39}_{-0.24}$ (stat) $\pm$ 0.09 (syst)
172	$1.03^{+0.50}_{-0.39}$ (stat) $\pm$ 0.09 (syst)
183	1.59 ± 0.26 (stat) $\pm$ 0.08 (syst)
189	1.86 ± 0.14 (stat) $\pm$ 0.04 (syst)
192	1.97 ± 0.37 (stat) $\pm$ 0.06 (syst)
196	1.87 ± 0.21 (stat) $\pm$ 0.05 (syst)
200	1.84 ± 0.20 (stat) $\pm$ 0.05 (syst)
202	1.81 ± 0.28 (stat) $\pm$ 0.05 (syst)
205	1.82 ± 0.20 (stat) $\pm$ 0.06 (syst)
207	1.82 ± 0.16 (stat) $\pm$ 0.06 (syst)

6 Systematic errors

A large variety of systematic effects were taken into account in the cross-section determination. They were due to imperfect modelling of the detector response or of underlying physics in the simulation, or to statistical uncertainties due to the finite size of the simulation samples.

Systematic errors were divided in three classes to facilitate their treatment in the combination of cross-section results from the four LEP experiments [29]: errors correlated between the experiments and between the different centre-of-mass energies (LCEC), typically due to the use of the same models to describe physics effects, errors uncorrelated between the experiments but correlated between centre-of-mass energies (LUEC), which comprise detector-related effects, and errors correlated neither between experiments nor between energies (LUEU) which are mainly due to uncertainties on simulation sample statistics. Correlations between the different channels were also taken into account.

Details of the determination of the systematic contributions are given in the following.

6.1 Estimation of systematic uncertainties

6.1.1 Background cross-sections from four-fermion and two-fermion processes

Theoretical uncertainties in the knowledge of four-fermion cross-sections largely depended on the process, varying

from ±2% in ZZ processes to ±5% in single-boson contributions. Larger uncertainties arose when considering regions of the phase space dominated by $\gamma\gamma$ collisions [29].

The four-fermion background generation was performed independently for charged and neutral current processes. The latter ones were further divided with phase space cuts to isolate as much as possible the contribution of multi-peripheral diagrams, where $\gamma\gamma$ scattering dominates, and which were generated in a complementary sample [17]. For the selected background from charged current processes, mainly the single-W contribution, a relative uncertainty of ±5% was assigned. The same uncertainty was used for the non-$\gamma\gamma$ neutral current background, with the exception of ZZ contributions where it became ±2%. For the remaining neutral current phase space a ±10% relative uncertainty was assigned.

The theory errors used for the two-fermion background cross-sections were those reported in [30]. A further uncertainty of ±1% was conservatively added to account for ungenerated regions of the phase space in the matching between two-fermion and four-fermion processes, where radiative corrections to $ee \to f\bar{f}$ could convert into an extra low-mass fermion pair.

The variations of each background were taken as fully correlated in channel and energy and the resulting change in the measured cross-section was quoted as a systematic error.

6.1.2 Modelling of four-jet background from $q\bar{q}$

In the fully hadronic channel the uncertainty on the background from two-fermion production leading to four-jet final states was estimated by comparing simulations with different hadronisation models, ARIADNE, PYTHIA and HERWIG. ARIADNE was chosen as default, because it provided the best description of the four-jet rates observed for the large data set at the Z peak [20] and also at LEP2 energies [31]. For the other models differences of $(-6.0 \pm 0.4)\%$ (PYTHIA) and $(+3.9 \pm 0.6)\%$ (HERWIG) were obtained for the background computation, and the largest difference of 6% was conservatively chosen as the systematic uncertainty. This estimate was confirmed by fitting all data to signal and background with a free parameter to scale the two-fermion background (ARIADNE), for which a change of $(4 \pm 3)\%$ was obtained.

6.1.3 Fragmentation modelling

Modelling of the fragmentation in hadronic events could have an impact both on the selection efficiency and on the background level estimated from the Monte Carlo. These effects were evaluated by comparing the performance of the selection algorithms on signal and background samples generated with different hadronisation models.

The PYTHIA hadronisation model, which best described the two-jet fragmentation at the Z peak, was taken as a reference to evaluate efficiencies for all channels and the background for the semi-leptonic channel. It was compared to ARIADNE [12] and HERWIG [13] and the largest deviations were considered to estimate the systematic errors on the cross-sections.

The largest variation in the signal efficiency was 0.58% in the fully hadronic channel and 1% in the semi-leptonic one, while the difference in the background level was found to be 3.2% in the semi-leptonic channel. For the hadronic channel this uncertainty is included in the four-jet modelling.

6.1.4 Final state interactions

At LEP2 energies the decay distance between the W bosons was smaller than the hadronisation scale or the typical radius where Bose-Einstein effects occur. Therefore gluon exchange between quarks from different Ws (known as Colour Reconnection) or Bose-Einstein Correlations between pions were to be expected. These so-called Final State Interactions (FSI) between the decay products of the two different Ws could affect the reconstruction of fully hadronic events only, and their modelling could have an impact on the determination of the selection efficiency.

The effects of Colour Reconnections and Bose-Einstein Correlations were estimated by evaluating the selection efficiency on simulation samples where FSI were modelled using the SK1 algorithm [32] with reconnection probability of 30% for Colour Reconnections and the LUBOEI algorithm [33] for Bose-Einstein Correlations. The full difference between the presence and the absence of these effects was taken as an indication of the systematic error, corresponding to a variation in efficiency of −0.3% and 0.2%, respectively.

6.1.5 Radiative corrections

The correct simulation of radiation in WW production and decay could be relevant for efficiency determination. Since the LEP2 Monte Carlo workshop [1], generators with a more precise calculation of $\mathcal{O}(\alpha)$ electroweak corrections to CC03 became available [16, 34]. The theoretical uncertainty on the total cross-section was reduced by almost a factor 4 down to a level of 0.5%, with a change of central value by almost 2% with respect to Gentle2.0 [35], run with parameter settings as described in [36]. Moreover, it was shown that the more correct description of electroweak corrections also had very important effects on differential distributions [37], making its inclusion essential for efficiency determinations.

The YFSWW [16] program was used in the generation for reweighting events according to the procedure described in [17]. In order to estimate the effect that theoretical uncertainty in the description of the radiation had on the selection efficiency, the results obtained in the DELPHI setup were compared with a simulation making use of RacoonWW [34] on the testbench process $u\bar{d}\mu\nu_\mu$. The two programs differed in many respects in the treatment of QED radiation: YFSWW was a $e^+e^- \to \mathrm{W}^+\mathrm{W}^- \to 4f$

generator (CC03 diagrams only) with $\mathcal{O}(\alpha)$ factorisable electroweak corrections and non-factorisable corrections implemented via the so-called Khoze-Chapovsky ansatz (KC) [38]. It included ISR in leading logarithm approximation (LL) $\mathcal{O}(\alpha^3)$ via YFS exponentiation [39] and final state radiation (FSR) LL $\mathcal{O}(\alpha^2)$ via PHOTOS [40]. On the other hand, RacoonWW was a $4f$ generator implementing $\mathcal{O}(\alpha)$ in Double Pole Approximation (DPA) rigorously, extended to $\mathcal{O}(\alpha^3)$ for collinear ISR via structure functions. It also included real corrections with the exact $e^+e^- \to 4f\gamma$ matrix elements of the CC11 [2] class.

The systematic uncertainty on the cross-section was estimated by comparing results from the two programs: no significant difference was found in the efficiencies, therefore the statistical error on this difference was taken as a conservative estimate of the systematic contribution.

6.1.6 Luminosity determination

The luminosity was determined from a measurement of Bhabha scattering, which was theoretically known to high accuracy. The measurement made use of coincidences in the very forward electromagnetic calorimeters and was affected by the experimental error on the acceptance ($\pm 0.5\%$). The residual theoretical uncertainty on the cross-section estimate was $\pm 0.12\%$ [41]. These uncertainties were propagated to a systematic error on σ_{WW}.

The statistical error on the Bhabha cross-section was included in the statistical error of the W-pair cross-section.

6.1.7 Detector effects

A non-perfect reproduction of track reconstruction and lepton identification efficiencies in the simulation could induce a systematic error on the signal efficiency and the background rejection. This was particularly relevant for semi-leptonic and fully leptonic channels.

These effects were evaluated from a comparison of the simulation with data on high statistics samples of clean two-lepton and two-jet events, which were collected at a centre-of-mass energy of 91.2 GeV. The data were taken with the same detector and trigger configuration and analysed with the same reconstruction software as the high energy data. High energy data samples were also used for the comparison, selecting events with a clean di-lepton and 2- or 3-jet topologies.

From data-simulation comparisons, corrections were deduced for the energies and polar angles of jets, and for the number of charged particle tracks in the endcap region. These led to corrections of the signal efficiency in the hadronic channel of $\pm 0.14\%$ (jets) and $\pm 0.30\%$ (endcap tracks), for which systematic uncertainties of $\pm 0.14\%$ and $\pm 0.10\%$ were assigned.

For lepton identification, the angular averaged difference in the identification efficiency between data and simulation of 0.3% for muons and 1% for electrons was found. The systematic error on the WW cross-section and W branching fractions was determined by randomly changing the lepton identification in the signal and background Monte Carlo according to the discrepancies found. The changes were correlated between the different channels. The effect on the total cross-section was small because most of the events lost as electrons or muons were recovered by the tau selections.

Other possible discrepancies between data and Monte Carlo in the variables used as inputs for the Neural Network in the hadronic channel were taken into account by smearing these variables in the simulation by their experimental resolution.

In total a systematic uncertainty of $\pm 0.55\%$ on the signal efficiency and $\pm 1.7\%$ on the total background was estimated for the hadronic channel. For the semi-leptonic channels the uncertainties on the signal efficiencies were $\pm 0.5\%$ for the $qqe\nu$ and $qq\mu\nu$ channels, and $\pm 1\%$ for the $qq\tau\nu$. The variations of the background ranged from 0.6% to 6% according to the channel. The systematic uncertainties in the fully leptonic channel were $\pm 1.5\%$ for the efficiency and 7% for the background.

6.1.8 Detector inefficiencies in a specific period

As mentioned in Sect. 2, one of the TPC sectors, covering 1/12 of the acceptance, was not operational during the last period of the high energy data taking in the year 2000. These data were analysed separately and then combined with the results from the previous period. The performance of the analyses and the cross-section values were found to be compatible within statistical errors. Additional systematic effects were estimated by comparing data collected at the Z peak during the period with the TPC sector 6 off with simulation samples produced with the same detector conditions. Both hadronic and leptonic Z decays were used. The impact on the WW cross-section analysis was conservatively evaluated as an uncertainty on the selection efficiency of $\pm 0.5\%$ in the fully hadronic channel and of 1% in the other channels, which was added to the systematic error. No effects were found on the background level.

6.1.9 Monte Carlo statistics

The uncertainties due to limited statistics of the Monte Carlo samples were at most $\pm 0.2\%$ on the signal efficiency and $\pm 2.0\%$ on the background level for the hadronic channels at energies above 172 GeV. The error on backgrounds in the fully leptonic channels were up to 10 times larger because of the small numbers of accepted events.

Table 9 presents the breakdown of the systematics per channel determined in the way described above for 200 GeV. The classification of the systematics according to their correlations in energy or experiments is also shown.

7 Differential cross-section

Given the high statistics available at LEP2, it is interesting to provide a measurement of differential cross-sections.

Table 9. Breakdown of systematic errors on the partial WW cross-sections at $\sqrt{s}$=200 GeV and their classification according to correlations between LEP experiments (LC) and between centre-of-mass energies (EC)

Source	$\sigma_{\mathrm{WW}}^{q\bar{q}q\bar{q}}$ (pb)	$\sigma_{\mathrm{WW}}^{q\bar{q}l\nu}$ (pb)	$\sigma_{\mathrm{WW}}^{l\nu l\nu}$ (pb)	LC	EC
Four-jet modelling	±0.051	±0.014	–	Y	Y
Background cross-sections	±0.009	±0.016	±0.006	Y	Y
Fragmentation	±0.045	±0.038	–	Y	Y
Final state interactions	±0.025	–	–	Y	Y
Radiative corrections	±0.008	±0.008	±0.002	Y	Y
Luminosity (theor)	±0.011	±0.010	±0.002	Y	Y
Luminosity (exp)	±0.045	±0.043	±0.011		Y
Detector effects	±0.045	±0.053	±0.033		Y
Monte Carlo statistics	±0.005	±0.014	±0.033		

Particularly relevant are the W polar angle distributions, from which triple gauge coupling limits can be extracted. In what follows the determination of $\mathrm{d}\sigma_{\mathrm{WW}}/\mathrm{dcos}\theta_{\mathrm{W}^-}$ is discussed.

The presented differential cross-section refer to CC03 $q\bar{q}e\nu$ and $q\bar{q}\mu\nu$ final states, since they give a clean W charge assignment, and has therefore to be understood as $\mathrm{d}[\sigma_{\mathrm{WW}}(\mathrm{BR}_{e\nu}+\mathrm{BR}_{\mu\nu})]/\mathrm{d}\cos\theta_{\mathrm{W}^-}$, where $\mathrm{BR}_{l\nu}$ is the branching ratio of the decay $\mathrm{WW}\to q\bar{q}l\nu$.

The IDA analysis described in Sect. 5.2.1 was used for the event selection; the W flight direction was determined via a constrained fit of the event which imposed four-momentum conservation and equality of the hadronic and leptonic invariant masses. In order to distinguish between radiation from Ws or from the final state fermions, the photon-to-fermion recombination scheme followed the CALO5 definition adopted in the LEP2 Monte Carlo workshop [1]. To match the detector acceptance best, an additional restriction requiring the charged lepton to be more than 20° away from the beam direction was introduced. For the $q\bar{q}e\nu$ case this additional cut strongly suppressed the contribution of single-W diagrams in the signal definition. The impact of possible systematic effects due to charge misidentification for leptons within the accepted angular region was found to be negligible from studies on dilepton events. To optimise the statistics in each bin, four bins in energy and ten bins in polar angle were chosen. Table 10 reports the energy binning, together with the corresponding luminosity and luminosity weighted centre-of-mass energy. The angular binning was chosen to be significantly bigger than the resolution on $\cos\theta_{\mathrm{W}^-}$, estimated to be about 0.06 from Monte Carlo, in order to minimise bin migration of data. The migration matrix, expressing the probability that an event selected in a certain bin was generated in another one, is reported in Appendix A. No corrections for bin migration were applied to the presented results. All the conventions used for presenting the DELPHI result, including signal and bin definitions, are the ones agreed for the LEP combination.

The results at the energies in Table 10 are reported in Fig. 5, where data points are superimposed on the expected distributions from WPHACT and YFSWW. The data are in agreement with the expectations in all energy ranges.

Table 10. Energies and luminosities in the bins for the differential cross-section measurement

Bin (GeV)	$\mathcal{L}$-weighted $\sqrt{s}$ (GeV)	$\mathcal{L}$ (pb^{-1})
180–184	182.65	51.63
184–194	189.03	178.32
194–204	198.46	193.52
204–210	205.91	198.59

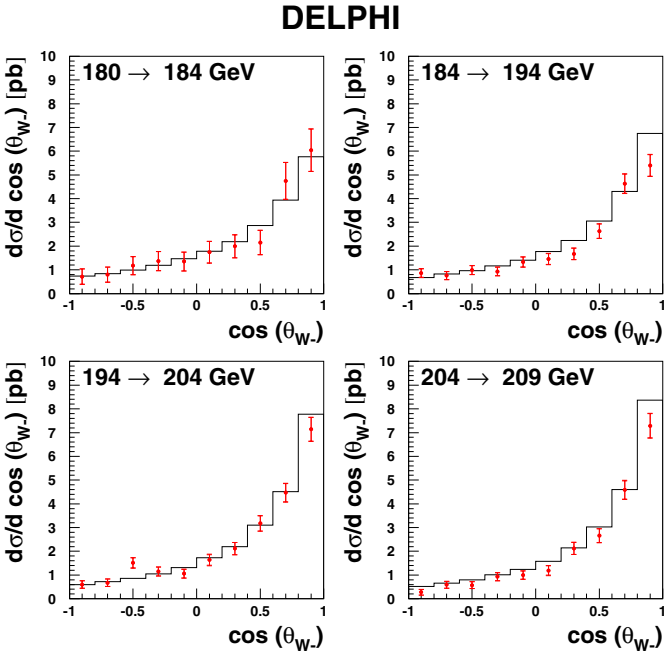

Fig. 5. W^- polar angle differential cross-sections from the $q\bar{q}e\nu$ and $q\bar{q}\mu\nu$ channels (detailed definition in the text). The measurements in the four energy bins defined in the text (points) are compared with the expectations (histograms). The systematic contributions are included in the error bars

A systematic deficit of data in the highest $\cos\theta_{\mathrm{W}^-}$ bin at energies above 184 GeV is observed. As a crosscheck, it was verified that the shape of the angular distributions, for electrons and muons separately, and for positively and negatively charged leptons, were compatible within errors.

Table 11. W branching fractions from data above 172 GeV and correlation matrix for the leptonic branching fractions

channel	branching fraction	stat. error	syst. error (LU)	syst. error (LC)
$W \to e\nu$	0.1055	0.0031	0.0013	0.0005
$W \to \mu\nu$	0.1065	0.0026	0.0006	0.0005
$W \to \tau\nu$	0.1146	0.0039	0.0017	0.0009

Correlations	$W \to e\nu$	$W \to \mu\nu$	$W \to \tau\nu$
$W \to e\nu$	1.00	0.03	−0.34
$W \to \mu\nu$	0.03	1.00	−0.17
$W \to \tau\nu$	−0.34	−0.17	1.00

	assuming lepton universality			
channel	branching fraction	stat. error	syst. error (LU)	syst. error (LC)
W → hadrons	0.6745	0.0041	0.0020	0.0014

The detailed list of results, in terms of measured cross-sections, statistical and systematic errors per bin is reported in Appendix A.

8 Determination of the W branching fractions and of the total WW production cross-section

The total cross-section for WW production and the W leptonic branching fractions were obtained from a likelihood fit based on the probabilities of finding the observed number of events in each final state. The input numbers in the form given in Tables 2 and 7 were used, except for the fully hadronic final state where, for energies above 172 GeV, the binned distribution of the neural network output was used.

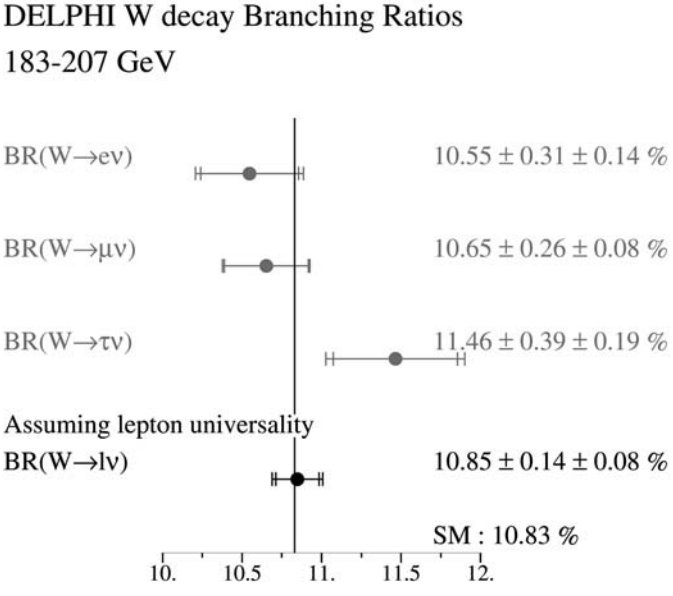

Fig. 6. W decay branching ratios (without and with the assumption of lepton universality) measured with the DELPHI data, in comparison with the Standard Model expectations [42]. Both the statistical and the total errors are indicated in the error bars

A fit without the assumption of lepton universality, requiring the unitarity of the branching ratios (i.e. $\mathrm{BR}_{e\nu} + \mathrm{BR}_{\mu\nu} + \mathrm{BR}_{\tau\nu} + \mathrm{BR}_{q\bar{q}'} = 1$), was performed. The results for all the data above 172 GeV are shown in Table 11. The analyses on the low statistics samples at 161 and 172 GeV used inclusive lepton identification. The correlation matrix is also reported, where both statistical and systematic contributions are included. Since the lepton branching ratios are in agreement, a second fit assuming lepton universality was performed in order to extract $\mathrm{BR}_{q\bar{q}'}$. The result for this second fit are also reported in Table 11. In Fig. 6 the results are compared to the Standard Model predictions. All results are consistent with the expectations and with lepton universality.

Within the Standard Model, the branching fractions of the W boson depend on the six matrix elements $|\mathrm{V_{qq'}}|$ of the Cabibbo–Kobayashi–Maskawa (CKM) quark mixing matrix not involving the top quark. In terms of these matrix elements, the leptonic branching fraction of the W boson $\mathrm{BR}_{l\nu}$ is given by

$$\frac{1}{BR_{l\nu}} = 3\left\{1 + \left[1 + \frac{\alpha_s(\mathrm{M_W^2})}{\pi}\right] \sum_{\substack{i=(u,c),\\ j=(d,s,b)}} |\mathrm{V}_{ij}|^2\right\},$$

where $\alpha_s(\mathrm{M_W^2})$ is the strong coupling constant. Taking $\alpha_s(\mathrm{M_W^2}) = 0.119 \pm 0.002$ [42], the measured leptonic branching fraction of the W yields

$$\sum_{\substack{i=(u,c),\\ j=(d,s,b)}} |\mathrm{V}_{ij}|^2 = 1.996 \pm 0.043\,(BR_{l\nu}) \pm 0.002\,(\alpha_s),$$

where the first error is due to the uncertainty on the branching fraction measurement and the second to the uncertainty on α_s. Using the experimental knowledge [42] of the sum $|\mathrm{V}_{ud}|^2 + |\mathrm{V}_{us}|^2 + |\mathrm{V}_{ub}|^2 + |\mathrm{V}_{cd}|^2 + |\mathrm{V}_{cb}|^2 = 1.0476 \pm 0.0074$,

Table 12. Measured total WW cross-sections. A breakdown of the systematic uncertainties in the different contributions, correlated between LEP experiments and/or between different centre-of-mass energies, is shown, according to the classification described in the text (see Sect. 6 for details)

$\sqrt{s}$ (GeV)	σ_{WW} (pb)	δ_σ (syst.) (pb)		
		LCEC	LUEU	LUEC
161	$3.61^{+0.97}_{-0.85}$ (stat) $\pm$ 0.19 (syst)	0.039	0.182	0.037
172	$11.37^{+1.44}_{-1.35}$ (stat) $\pm$ 0.32 (syst)	0.115	0.288	0.095
183	16.07 $\pm$ 0.68 (stat) $\pm$ 0.16 (syst)	0.100	0.044	0.126
189	16.09 $\pm$ 0.39 (stat) $\pm$ 0.16 (syst)	0.094	0.028	0.127
192	16.64 $\pm$ 0.99 (stat) $\pm$ 0.17 (syst)	0.103	0.040	0.131
196	17.04 $\pm$ 0.58 (stat) $\pm$ 0.17 (syst)	0.100	0.033	0.133
200	17.39 $\pm$ 0.55 (stat) $\pm$ 0.17 (syst)	0.102	0.029	0.135
202	17.37 $\pm$ 0.79 (stat) $\pm$ 0.17 (syst)	0.107	0.030	0.136
205	17.56 $\pm$ 0.57 (stat) $\pm$ 0.17 (syst)	0.107	0.039	0.136
207	16.35 $\pm$ 0.44 (stat) $\pm$ 0.17 (syst)	0.103	0.051	0.128

the results of Table 11 can be interpreted as a measurement of $|V_{cs}|$ which is the least well determined of these matrix elements:

$$|V_{cs}| \quad = \quad 0.973 \pm 0.019(\mathrm{stat}) \pm 0.012(\mathrm{syst})$$

where the uncertainties on the SM parameters are included in the systematic error.

If the SM values of the W branching ratio [42] are assumed, the fitting procedure can be repeated with the total WW production cross-sections as the only free parameter. The results obtained from all the data samples are reported in Table 12. In this table the breakdown of the systematic contributions into the correlation categories defined in Table 9 is also shown. Correlations between the different channels were also taken into account.

A comparison of the results with the most recent calculations in the Double Pole Approximation from RacoonWW and YFSWW is shown in Fig. 7. As DPA computations are not reliable close to the WW threshold, the predictions below 168 GeV were obtained running those programs in the Improved Born Approximation (IBA), which only accounts for initial state radiation and Coulomb corrections. The shaded region represents the theoretical uncertainty of the calculations and was obtained by an analytic parametrisation of the relative uncertainty given in [1]. This led to an accuracy on the theoretical curves of about $\pm 0.7\%$ at 168 GeV and of $\pm 0.4\%$ at 200 GeV. The uncertainties from RacoonWW and from YFSWW were merged into a single error band.

The measurements are in very good agreement with the Standard Model expectations.

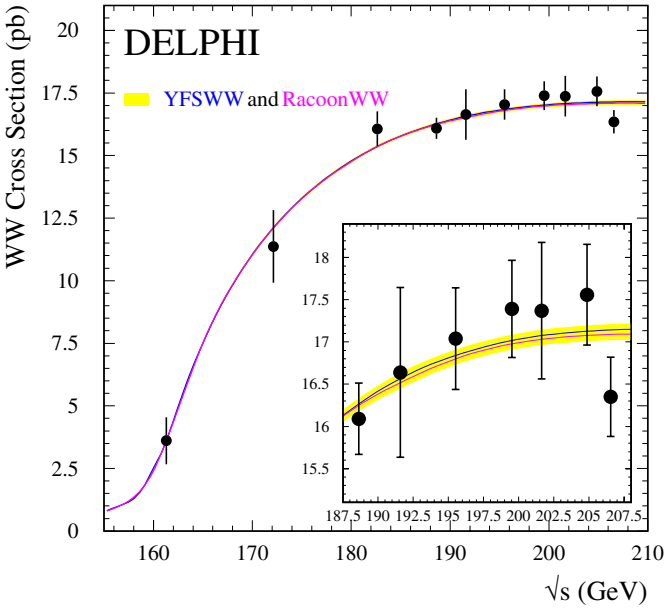

Fig. 7. Measurements of the WW cross-section compared with the Standard Model prediction given by the YFSWW [16] and RacoonWW [34] programs. The shaded band represents the uncertainty on the theoretical calculations

9 Determination of $\mathcal{R}_{\mathrm{WW}}$

The cross-section measurements for different energies can be combined into a single value to quantify the overall agreement with theoretical predictions. $\mathcal{R}_{\mathrm{WW}}$ is defined as the ratio between the experimentally determined cross-section and the theoretical expectations. This procedure was used to compare the measurements at the eight energies between 183 and 207 GeV to the predictions of Gentle, KoralW, YFSWW and RacoonWW. The measurements at 161 and 172 GeV were not used because of the high sensitivity of the cross-section to the value of the W mass at these energies.

For each calculation, the cross-sections were converted into ratios by dividing them by the corresponding theoretical predictions, and combined taking into account the energy correlation of the systematics.

Table 13. $\mathcal{R}_{\mathrm{WW}}$ values from the combination of all the data, using different theoretical calculations

Theoretical prediction	$\mathcal{R}_{\mathrm{WW}}$
Gentle 2.0	0.974 ± 0.015 (exp) ± 0.019(theo)
KoralW	0.979 ± 0.015 (exp) ± 0.010(theo)
YFSWW	0.999 ± 0.015 (exp) ± 0.005(theo)
RacoonWW	1.001 ± 0.015 (exp) ± 0.005(theo)

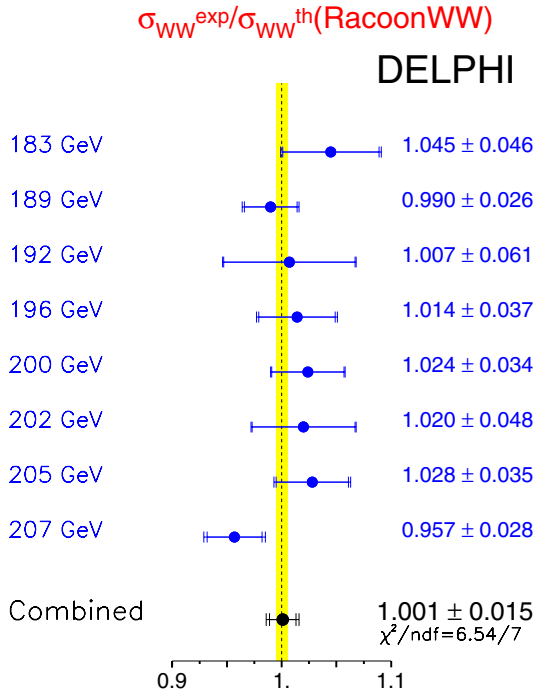

Fig. 8. Ratios between measured and predicted CC03 cross-sections with the DELPHI data. The error bars indicate the combined statistical and systematic uncertainties. The energy-combined values are indicated at the bottom. The plot refers to the RacoonWW predictions, where a 0.5% theory error is indicated as a band

The theoretical errors on the calculations, due to both physical and technical precision of the generators used, were also propagated to the ratios.

The values of $\mathcal{R}_{\mathrm{WW}}$ at the various centre-of-mass energies are presented in Fig. 8 for the RacoonWW calculation. The band on the figure represents the theoretical error on the prediction, where its dependence on energy is ignored for simplicity. The $\mathcal{R}_{\mathrm{WW}}$ values from the combination of all the data using different theoretical calculations are shown in Table 13. Both statistical and systematic contributions are indicated. It is worth noting how the estimated theory error (taken from [1], page 34) decreases from Gentle to RacoonWW and that the final experimental precision on $\mathcal{R}_{\mathrm{WW}}$ with the DELPHI data at LEP2 approaches ±1.5%, to be compared with ±0.5% from the best theory computations. The data favour the more complete inclusion of radiative corrections in the calculation at the level of 1.5 σ.

10 Conclusions

The WW production cross-section from e^+e^- annihilations has been measured at ten centre-of-mass energies between 161 and 209 GeV with the DELPHI experiment at LEP. The data correspond to a total integrated luminosity of about 670 pb^{-1}.

The results are in agreement with the predictions of the most recent CC03 cross-section calculations and test them to an accuracy of about 1.5%.

Differential distributions in the polar angle of the reconstructed W are also measured in the semileptonic channels.

The W branching fractions are measured with an uncertainty of less than ±4% for individual leptons and about ±0.7% for hadrons. They also agree with the Standard Model expectation. From the leptonic branching fraction a precise determination of $|V_{cs}|$ is derived.

Acknowledgements. We are greatly indebted to our technical collaborators, to the members of the CERN-SL Division for the excellent performance of the LEP collider, and to the funding agencies for their support in building and operating the DELPHI detector. We acknowledge in particular the support of Austrian Federal Ministry of Education, Science and Culture, GZ 616.364/2-III/2a/98, FNRS–FWO, Flanders Institute to encourage scientific and technological research in the industry (IWT), Federal Office for Scientific, Technical and Cultural affairs (OSTC), Belgium, FINEP, CNPq, CAPES, FUJB and FAPERJ, Brazil, Czech Ministry of Industry and Trade, GA CR 202/99/1362, Commission of the European Communities (DG XII), Direction des Sciences de la Matière, CEA, France, Bundesministerium für Bildung, Wissenschaft, Forschung und Technologie, Germany, General Secretariat for Research and Technology, Greece, National Science Foundation (NWO) and Foundation for Research on Matter (FOM), The Netherlands, Norwegian Research Council, State Committee for Scientific Research, Poland, SPUB-M/CERN/PO3/DZ296/2000, SPUB-M/CERN/PO3/DZ297/2000 and 2P03B 104 19 and 2P03B 69 23(2002–2004) JNICT–Junta Nacional de Investigação Científica e Tecnológica, Portugal, Vedecka grantova agentura MS SR, Slovakia, Nr. 95/5195/134, Ministry of Science and Technology of the Republic of Slovenia, CICYT, Spain, AEN99-0950 and AEN99-0761, The Swedish Natural Science Research Council, Particle Physics and Astronomy Research Council, UK, Department of Energy, USA, DE-FG02-01ER41155, EEC RTN contract HPRN-CT-00292-2002.

Appendix A: Results on W polar angle measurements

The details of the results for the measurement of the W^- polar angle differential cross-section are reported in Table 14. For convenience the integrated luminosities and the lumosity-weighted centre-of-mass energies in each of the energy bins defined in the text are also provided.

Table 15 presents the signal event migration matrix determined from the Monte Carlo. The Standard Model W polar angle differential distribution is therefore implicitly assumed.

Table 14. Differential cross-sections in the 10 angular bins for the four energy intervals (see descriptions in Sect. 7). σ_i indicates the average of $\mathrm{d}[\sigma_{\mathrm{WW}}(\mathrm{BR}_{e\nu}+\mathrm{BR}_{\mu\nu})]/\mathrm{d}\cos\theta_{\mathrm{W}^-}$ in the i-th bin of $\cos\theta_{\mathrm{W}^-}$ with width 0.2. The limits of the bins are also reported in the table. The values, in each bin, of the measured and expected statistical error and of the systematic errors due to the background and to the efficiencies are reported as well. All systematic errors have to be considered correlated in energy and bin. All values are expressed in pb

	180–184 GeV		184–194 GeV		194–204 GeV		204–210 GeV	
$\mathcal{L}$ (pb^{-1})	51.63		178.32		193.52		198.59	
weighted $\sqrt{s}$ (GeV)	182.65		189.03		198.46		205.91	
σ_1 [-1,-0.8)	0.715		0.865		0.600		0.275	
$\delta\sigma_1^{\mathrm{stat.}}$(meas) $\delta\sigma_1^{\mathrm{stat.}}$(exp)	0.320	0.320	0.180	0.165	0.155	0.150	0.120	0.145
$\delta\sigma_1^{\mathrm{syst.}}$(back) $\delta\sigma_1^{\mathrm{syst.}}$(eff)	0.045	0.020	0.040	0.020	0.025	0.015	0.020	0.015
σ_2 [-0.8,-0.6)	0.795		0.760		0.675		0.590	
$\delta\sigma_2^{\mathrm{stat.}}$(meas) $\delta\sigma_2^{\mathrm{stat.}}$(exp)	0.315	0.315	0.170	0.170	0.160	0.160	0.145	0.150
$\delta\sigma_2^{\mathrm{syst.}}$(back) $\delta\sigma_2^{\mathrm{syst.}}$(eff)	0.025	0.025	0.020	0.020	0.015	0.020	0.015	0.020
σ_3 [-0.6,-0.4)	1.175		0.990		1.510		0.575	
$\delta\sigma_3^{\mathrm{stat.}}$(meas) $\delta\sigma_3^{\mathrm{stat.}}$(exp)	0.380	0.350	0.185	0.180	0.215	0.170	0.140	0.160
$\delta\sigma_3^{\mathrm{syst.}}$(back) $\delta\sigma_3^{\mathrm{syst.}}$(eff)	0.020	0.035	0.020	0.035	0.015	0.030	0.010	0.025
σ_4 [-0.4,-0.2)	1.365		0.930		1.150		0.930	
$\delta\sigma_4^{\mathrm{stat.}}$(meas) $\delta\sigma_4^{\mathrm{stat.}}$(exp)	0.400	0.370	0.180	0.200	0.190	0.180	0.170	0.175
$\delta\sigma_4^{\mathrm{syst.}}$(back) $\delta\sigma_4^{\mathrm{syst.}}$(eff)	0.015	0.035	0.015	0.035	0.015	0.035	0.010	0.035
σ_5 [-0.2,0)	1.350		1.330		1.055		1.000	
$\delta\sigma_5^{\mathrm{stat.}}$(meas) $\delta\sigma_5^{\mathrm{stat.}}$(exp)	0.400	0.405	0.215	0.215	0.185	0.200	0.175	0.195
$\delta\sigma_5^{\mathrm{syst.}}$(back) $\delta\sigma_5^{\mathrm{syst.}}$(eff)	0.015	0.040	0.015	0.040	0.015	0.035	0.015	0.035
σ_6 [0,0.2)	1.745		1.460		1.635		1.190	
$\delta\sigma_6^{\mathrm{stat.}}$(meas) $\delta\sigma_6^{\mathrm{stat.}}$(exp)	0.450	0.450	0.225	0.240	0.225	0.230	0.195	0.220
$\delta\sigma_6^{\mathrm{syst.}}$(back) $\delta\sigma_6^{\mathrm{syst.}}$(eff)	0.025	0.085	0.020	0.085	0.015	0.085	0.010	0.085
σ_7 [0.2,0.4)	1.995		1.675		2.115		2.120	
$\delta\sigma_7^{\mathrm{stat.}}$(meas) $\delta\sigma_7^{\mathrm{stat.}}$(exp)	0.485	0.505	0.240	0.270	0.255	0.260	0.255	0.250
$\delta\sigma_7^{\mathrm{syst.}}$(back) $\delta\sigma_7^{\mathrm{syst.}}$(eff)	0.015	0.050	0.015	0.050	0.010	0.045	0.010	0.045
σ_8 [0.4,0.6)	2.150		2.630		3.175		2.655	
$\delta\sigma_8^{\mathrm{stat.}}$(meas) $\delta\sigma_8^{\mathrm{stat.}}$(exp)	0.510	0.580	0.300	0.320	0.320	0.310	0.290	0.300
$\delta\sigma_8^{\mathrm{syst.}}$(back) $\delta\sigma_8^{\mathrm{syst.}}$(eff)	0.015	0.065	0.015	0.060	0.015	0.055	0.010	0.055
σ_9 [0.6,0.8)	4.750		4.635		4.470		4.585	
$\delta\sigma_9^{\mathrm{stat.}}$(meas) $\delta\sigma_9^{\mathrm{stat.}}$(exp)	0.775	0.695	0.405	0.385	0.385	0.380	0.385	0.380
$\delta\sigma_9^{\mathrm{syst.}}$(back) $\delta\sigma_9^{\mathrm{syst.}}$(eff)	0.030	0.095	0.025	0.100	0.025	0.105	0.020	0.110
σ_{10} [0.8,1]	6.040		5.400		7.140		7.290	
$\delta\sigma_{10}^{\mathrm{stat.}}$(meas) $\delta\sigma_{10}^{\mathrm{stat.}}$(exp)	0.895	0.850	0.455	0.490	0.500	0.505	0.505	0.520
$\delta\sigma_{10}^{\mathrm{syst.}}$(back) $\delta\sigma_{10}^{\mathrm{syst.}}$(eff)	0.035	0.075	0.035	0.085	0.030	0.100	0.030	0.110

Table 15. Polar angle migration matrix at 200 GeV for selected events of the signal, according to the definition described in the text. The matrix is defined as $M_{ij} = N_{seli;genj}/N_{seli}$, where $N_{seli;genj}$ is the number of events selected in bin i and generated in bin j and N_{seli} is the total number of events selected in bin i. The numbers are all expressed in percent. By construction the rows sum up to 100%. The relative errors on the numbers on the diagonal are below 2%, whereas outside the diagonal they reach 7%

	gen 1	gen 2	gen 3	gen 4	gen 5	gen 6	gen 7	gen 8	gen 9	gen 10
sel 1	71.8	13.4	2.1	1.3	0.5	0.4	0.1	0.5	1.8	8.0
sel 2	11.4	61.7	15.4	2.7	2.1	0.8	0.6	0.7	2.4	2.2
sel 3	1.5	12.2	57.2	16.7	4.2	1.5	1.4	1.8	2.1	1.3
sel 4	0.8	1.9	11.7	58.9	16.8	4.1	2.6	1.5	0.9	0.8
sel 5	0.2	0.5	1.7	12.8	56.4	18.9	5.0	2.4	1.1	1.0
sel 6	0.2	0.2	0.4	1.8	12.9	58.8	18.7	3.9	1.9	1.3
sel 7	0.1	0.1	0.4	0.6	1.7	12.0	59.8	19.9	4.0	1.5
sel 8	0.0	0.1	0.1	0.3	0.5	1.7	11.6	63.3	19.4	3.2
sel 9	0.1	0.0	0.1	0.1	0.2	0.4	0.9	9.9	70.7	17.6
sel 10	0.1	0.0	0.0	0.0	0.1	0.1	0.2	0.7	7.4	91.4

References

1. M. Grünewald et al., Four-Fermion Production in Electron-Positron Collisions, in Report of the Working Groups on precision calculations for LEP2 physics, ed. S. Jadach et al., CERN 2000-009, 1 (2000)[hep-ph/0005309]
2. W. Beenakker, F. A. Berends et al., WW Cross-Section and Distributions, Physics at LEP2, eds. G. Altarelli, T. Sjöstrand and F. Zwirner, CERN 96-01 (1996) Vol. 1, 79
3. DELPHI Collaboration, P. Aarnio et al., Nucl. Instr. and Meth. A **303**, 233 (1991); DELPHI Collaboration, P. Abreu et al., Nucl. Instr. and Meth. A **378**, 57 (1996)
4. The DELPHI trigger group, A. Augustinus et al., CERN-EP 2002-082, submitted to NIM A
5. The DELPHI Silicon Tracker Group, P. Chochula et al., Nucl. Instr. and Meth. A **412**, 304 (1998)
6. S. J. Alvsvaag et al., Nucl. Instr. and Meth. A **425**, 106 (1999)
7. DELPHI Collaboration, P. Abreu et al., Phys. Lett. B **479**, 89 (2000)
8. DELPHI Collaboration, P. Abreu et al., Phys. Lett. B **456**, 310 (1999)
9. DELPHI Collaboration, P. Abreu et al., Eur. Phys. J. C **2**, 581 (1998); Phys. Lett. B **397**, 158 (1997)
10. E. Accomando and A. Ballestrero, Comp. Phys. Comm. **99**, 270 (1997); E. Accomando, A. Ballestrero and E. Maina, Comp. Phys. Comm. **150**, 166 (2003)
11. T. Sjöstrand, PYTHIA 5.719 / JETSET 7.4, Physics at LEP2, eds. G. Altarelli, T. Sjöstrand and F. Zwirner, CERN 96-01 (1996) Vol. 2, 41; T. Sjöstrand et al., Comp. Phys. Comm. **135**, 238 (2001)
12. L. Lönnblad, Comp. Phys. Comm. **71**, 15 (1992)
13. G. Corcella et al., Comp. Phys. Comm. **67**, 465 (1992)
14. F.A. Berends, P.H. Daverveldt and R. Kleiss, Comp. Phys. Comm. **40**, 285 (1986)
15. F.A. Berends, P.H. Daverveldt and R. Kleiss, Comp. Phys. Comm. **40**, 271 (1986)
16. S. Jadach, W. Placzek, M. Skrzypek, B.F.L. Ward and Z. Was, Comp. Phys. Comm. **140**, 432 (2001)
17. A. Ballestrero, R. Chierici, F. Cossutti and E. Migliore, Comp. Phys. Comm. **152**, 175 (2003)
18. S. Jadach, B.F.L. Ward and Z. Was, Comp. Phys. Comm. **130**, 260 (2000)
19. S. Jadach, B.F.L. Ward and Z. Was, Comp. Phys. Comm. **79**, 503 (1994)
20. DELPHI Collaboration, P. Abreu et al., Zeit. Phys. C **73**, 11 (1996)
21. S. Jadach, W. Placzek and B.F.L. Ward, Phys. Lett. B **390**, 298 (1997)
22. S. Catani et al., Phys. Lett. B **269**, 432 (1991)
23. P. Abreu et al, Nucl. Instr. and Meth. A **427**, 487 (1999)
24. C. Peterson, T. Rögnvaldsson, L. Lönnblad, Comp. Phys. Comm. **81**, 185 (1994)
25. K.-H. Becks, J. Drees, U. Flagmeyer and U. Müller, Nucl. Instr. and Meth. A **426**, 599 (1999)
26. G.C. Fox and S. Wolfram, Nucl. Phys. B **149**, 413 (1979); Erratum-ibid. B **157**, 543 (1979)
27. T.G.M. Malmgren, Comp. Phys. Comm. **106**, 230 (1997)
28. MLPfit, written by J. Schwindling, B. Mansoulié and O. Couet. More information in http://schwind.home.cern.ch/schwind/MLPfit.html
29. The LEP WW Working Group, LEPEWWG/2002-02, available from http://lepewwg.web.cern.ch/LEPEWWG/Welcome.html
30. F. Boudjema, B. Mele et al., Standard Model Processes, Physics at LEP2, eds. G. Altarelli, T. Sjöstrand and F. Zwirner, CERN 96-01 (1996) Vol. 1, 207
31. U.Flagmeyer et al, Contributed paper for EPS HEP 2001 (Budapest) and LP01 (Rome), DELPHI 2001-059 CONF 487 (2001), publication in preparation
32. T. Sjöstrand and V.A. Khoze, Z. Phys. C **62**, 281 (1994)
33. L.Lönnblad, T.Sjöstrand, Eur. Phys. J. C **2**, 165 (1998)
34. A. Denner et al., Phys. Lett. B **475**, 127 (2000)
35. D. Bardin et al., Comp. Phys. Comm. **104**, 161 (1997)
36. D. Bardin, R. Kleiss et al., in Physics at LEP2, G. Altarelli, T. Sjöstrand and F. Zwirner eds., CERN 96-01 (1996), Vol. 2, pg 3. hep-ph/9709270
37. R. Chierici and F. Cossutti, Eur. Phys. J. C **23**, 65 (2002)
38. A.P. Chapovsky and V.A. Khoze, Eur. Phys. J. C **9**, 449 (1999)
39. D. R. Yennie, S. C. Frautschi, H. Suura, Annals of Phys. **13**, 379 (1961)
40. E. Barberio, B. van Eijk and Z Was, Comput. Phys. Commun. **66**, 115 (1991),
    E. Barberio and Z. Was, Comp. Phys. Comm. **79**, 291 (1994)
41. W. Placzek et al., CERN-TH 99-07 and hep-ph/9903381
42. K. Hagiwara et al., Phys. Rev. D **66**, 010001 (2002)